Nonlinear simulations of beam-driven compressional Alfvén eigenmodes in NSTX

E. V. Belova, N. N. Gorelenkov, N. A. Crocker, J. B. Lestz, E. D. Fredrickson, S. Tang, and K. Tritz

---

Articles you may be interested in

Electron holes in phase space: What they are and why they matter
Physics of Plasmas **24**, 055601 (2017); 10.1063/1.4976854

Multi-region relaxed magnetohydrodynamics in plasmas with slowly changing boundaries—Resonant response of a plasma slab
Physics of Plasmas **24**, 042507 (2017); 10.1063/1.4979350

Fast-ion transport by Alfvén eigenmodes above a critical gradient threshold
Physics of Plasmas **24**, 056109 (2017); 10.1063/1.4977535

Symmetry breaking of ion temperature gradient mode structure: From local to global analysis
Physics of Plasmas **24**, 042502 (2017); 10.1063/1.4978947

Destabilization of toroidal Alfvén eigenmode during neutral beam injection heating on HL-2A
Physics of Plasmas **24**, 042509 (2017); 10.1063/1.4979892

Formation of solitary waves and oscillatory shocklets in a two-temperature electron κ–distributed plasma
Physics of Plasmas **24**, 042109 (2017); 10.1063/1.4979675

CrossMark
click for updates

Nonlinear simulations of beam-driven compressional Alfvén eigenmodes in NSTX

E. V. Belova,[1,a)] N. N. Gorelenkov,[1] N. A. Crocker,[2] J. B. Lestz,[1] E. D. Fredrickson,[1] S. Tang,[2] and K. Tritz[1]

[1]*Princeton Plasma Physics Laboratory, P. O. Box 451, Princeton, NJ 08543, USA*
[2]*University of California, Los Angeles, California 90095, USA*

Results of 3D nonlinear simulations of neutral-beam-driven compressional Alfvén eigenmodes (CAEs) in the National Spherical Torus Experiment (NSTX) are presented. Hybrid MHD-particle simulations for the H-mode NSTX discharge (shot 141398) using the HYM code show unstable CAE modes for a range of toroidal mode numbers, $n = 4 - 9$, and frequencies below the ion cyclotron frequency. It is found that the essential feature of CAEs is their coupling to kinetic Alfvén wave (KAW) that occurs on the high-field side at the Alfvén resonance location. High-frequency Alfvén eigenmodes are frequently observed in beam-heated NSTX plasmas, and have been linked to flattening of the electron temperature profiles at high beam power. Coupling between CAE and KAW suggests an energy channeling mechanism to explain these observations, in which beam-driven CAEs dissipate their energy at the resonance location, therefore significantly modifying the energy deposition profile. Nonlinear simulations demonstrate that CAEs can channel the energy of the beam ions from the injection region near the magnetic axis to the location of the resonant mode conversion at the edge of the beam density profile. A set of nonlinear simulations show that the CAE instability saturates due to nonlinear particle trapping, and a large fraction of beam energy can be transferred to several unstable CAEs of relatively large amplitudes and absorbed at the resonant location. Absorption rate shows a strong scaling with the beam power. *Published by AIP Publishing.* [http://dx.doi.org/10.1063/1.4979278]

I. INTRODUCTION

Flattening of electron temperature profiles and anomalously low central temperature at high beam power in the National Spherical Torus Experiment (NSTX) have been linked with strong activity of Alfvén modes in the sub-cyclotron frequency range.[1] The reduced heating of the plasma core in NSTX can significantly limit plasma performance, and potentially can have important implications for future fusion devices, especially low aspect ratio tokamaks. Modes in the sub-cyclotron frequency range are frequently observed during neutral beam injection (NBI) in NSTX, and they were identified as compressional Alfvén eigenmodes (CAEs) and global Alfvén eigenmodes (GAEs), driven unstable through the resonance with the super Alfvénic NBI ions.[2–4] The GAE in toroidal geometry is characterized by shear Alfvén wave polarization and frequency below the minimum of the Alfvén continuum,[5–8] and the CAE is a fast magnetosonic eigenmode.[9–11]

Previous theoretical studies attributed flattening of the electron temperature profile to an enhanced electron transport due to sub-cyclotron frequency Alfvén modes. Several mechanisms have been suggested, including interaction of Alfvén eigenmodes with bulk electrons via parallel electric field, as well as stochasticity of the electron orbits in the presence of multiple unstable and overlapping GAE modes of sufficiently large amplitudes.[12] However, other estimates[13] suggest that

AE-induced transport should have a minor effect, but the energy channeling from core-localized GAEs to continuum damping closer to the edge can be responsible for the observed flattening of the electron temperature profiles. This paper presents results of nonlinear self-consistent simulations of neutral-beam-driven CAEs, which support an alternative, the energy channeling mechanism originally proposed in Ref. 14. Three-dimensional hybrid MHD-particle simulations show that an essential feature of CAEs is their coupling to kinetic Alfvén waves (KAW) that occurs on the high-field side (HFS) at the Alfvén resonance location. The beam-driven CAE can mode-convert to KAW, channelling energy from the beam ions at the injection region near the magnetic axis to the location of the resonant mode conversion at the edge of the beam density profile. This mechanism can explain the reduced heating of the plasma core in NSTX. It is also shown that strong CAE/KAW coupling follows from the dispersion relation, and will occur for unstable CAEs in other toroidal devices. This paper extends the previous work,[14] and presents the results of a set of nonlinear simulations, which quantify resonant power absorption. The CAE instability drive and mode structure are investigated in detail, and results of beam ion parameter scan are presented.

Fast wave conversion and absorption at the Alfvén resonance have been known previously, and studied in applications to space plasma physics,[15–18] as well as tokamak plasmas.[19–22] It was found that the compressional wave can mode convert into KAW with amplitude enhanced compared with the driving compressional wave at the Earth's magnetopause.[16] Hybrid

a)ebelova@pppl.gov

simulations in a 2D box geometry investigated mode conversion of an incident fast mode to KAWs,[17] and beam-ion-driven compressional wave mode conversion to KAWs[18] in nonuniform plasmas.

Fast wave conversion has also been investigated extensively in relation to ion cyclotron resonance heating (ICRH)[21,22] and Alfvén wave heating.[15] Analytical and numerical studies of the fast wave heating in tokamak plasmas found that mode conversion can be an important parasitic damping mechanism.[21,22] It was shown that a conversion of an antenna-driven fast wave to shear Alfvén wave can take place on HFS near the plasma boundary in a small aspect ratio tokamak. One-dimensional calculation indicates that a relatively large fraction of the power (20%–40%) can be mode converted, resulting in a parasitic damping near the edge.[21] The change in the Poynting flux across the resonance has been shown to scale with plasma density, and mode parameters, and stronger absorption has been predicted at the resonances situated further inside plasma,[21] where the density is higher, and the scale lengths are larger. Comparison of full-wave equations with a 2-fluid model has demonstrated the importance of the parallel electron dynamics.[22] Importance of finite-frequency effects (ω/ω_{ci}) on resonant absorption was also considered in Refs. 19 and 20.

The problem of CAE to KAW conversion considered here is different to some degree from the previous studies, because the CAE is a beam-driven eigenmode, which can be described as a standing wave in the poloidal plane, rather than an incoming wave driven by an antenna. Three-dimensional self-consistent simulations show multiple unstable CAEs for a range of toroidal mode numbers, coupled with KAW on the high field side. Linearized simulations show that the coupling to KAW is the main damping mechanism for CAEs. The numerical model in the HYM code allows a full kinetic description of the beam ions, including the cyclotron resonances, but a one fluid MHD description is used to model the thermal plasma; therefore, the radial width of KAW is determined by the beam ion Larmor radius. The numerical model and results of linearized simulations for different toroidal mode numbers are described in Sections II–IV. Both experimental observations and numerical simulations presented here demonstrate that for this particular H-mode NSTX discharge a large number of GAEs and CAEs were excited by the beam ions. The calculated range of the unstable toroidal mode numbers, frequencies, and mode polarizations are compared with experimental observations[23,24] in Section III. Section IV focuses on the linear properties of CAE/KAW, and resonant beam ion drive. Results of fully nonlinear simulations are described in Sections V and VI, where possible effects of CAE/KAW coupling on the electron temperature profiles in the NSTX are discussed.

II. MODEL/CODE DESCRIPTION

The hybrid code HYM[25–27] has been used to investigate properties of beam ion driven sub-cyclotron frequency Alfvén modes in NSTX. The HYM code is a 3D nonlinear, global stability code in toroidal geometry, which treats the beam ions using full-orbit, delta-f particle simulations, while the one-fluid resistive MHD model is used to represent the background plasma. The two plasma components are coupled using a current coupling scheme. In this scheme, the momentum equation for the thermal plasma is:

$$\rho d\mathbf{V}/dt = -\nabla p + (\mathbf{J} - \mathbf{J}_b) \times \mathbf{B}/c - qn_b(\mathbf{E} - \eta\delta\mathbf{J}) + \nu\Delta\mathbf{V} \tag{1}$$

where ρ, $\mathbf{V}$, and p are the thermal plasma density, velocity, and pressure, respectively; n_b and $\mathbf{J}_b$ are the beam ion density and the beam ion induced current, respectively; $\mathbf{J} = c/4\pi\nabla \times\mathbf{B}$ is the total plasma current; $\delta\mathbf{J} = c/4\pi\nabla \times \delta\mathbf{B}$ and $\delta\mathbf{B}$ are perturbed current density and perturbed magnetic field, respectively; and ν is a viscosity coefficient. Equation (1) can be obtained by adding momentum equations for the thermal ions with density n_i and thermal electrons, neglecting the electron inertia, and using a quasineutrality condition: $n_e = n_b + n_i$.

The rest of the fluid equations are:

$$\mathbf{E} = -\mathbf{V} \times \mathbf{B}/c + \eta\delta\mathbf{J},$$
$$\frac{\partial\mathbf{B}}{\partial t} = -c\nabla \times \mathbf{E},$$
$$\mathbf{J} = c/4\pi\nabla \times \mathbf{B},$$
$$\frac{\partial\rho}{\partial t} = -\nabla \cdot (\mathbf{V}\rho)$$
$$\frac{\partial p}{\partial t} + \mathbf{V} \cdot \nabla p + \gamma p\nabla \cdot \mathbf{V} = (\gamma - 1)\Big[\eta\mathbf{J} \cdot \delta\mathbf{J} + \nu(\nabla \times \mathbf{V})^2$$
$$+\nu(\nabla \cdot \mathbf{V})^2\Big]. \tag{2}$$

Here $\mathbf{E}$ is the perturbed electric field, $\mathbf{B}$ is the total magnetic field, the pressure equation includes Ohmic and viscous heating, and $\gamma = 5/3$. It is assumed that the fast ion pressure can be comparable to that of the thermal plasma, but the beam ions have a low density $n_b \ll n_e$. In this case, the MHD Ohm's law (2) applies.

Energy conservation for this system can be written as:

$$\frac{dE_{tot}}{dt} = \oint\left[c\frac{\mathbf{B} \times \mathbf{E}}{4\pi} - \rho\frac{V^2}{2}\mathbf{V} - \frac{\gamma}{\gamma - 1}p\mathbf{V} - \int m_i\frac{v^2}{2}\mathbf{v}F \, d^3\mathbf{v}\right]ds,$$

where the total energy is the sum of the fluid energy (magnetic field and thermal plasma) and the beam ion energy:

$$E_{tot} = \int\left(\frac{B^2}{8\pi} + \frac{p}{\gamma - 1} + \rho\frac{V^2}{2}\right)d^3\mathbf{x} + \int m_i\frac{v^2}{2}F \, d^3\mathbf{v}d^3\mathbf{x},$$

and F is the beam ion distribution function.

The beam ions are described as kinetic particles using PIC simulation method and full-orbit equations of motion. The delta-f method[28] is used to reduce numerical noise in the simulations. In this method, the equilibrium distribution function of NBI ions needs to be known analytically, and the equation for the perturbed distribution function $\delta F = F - F_0$ is integrated along the particle trajectories:

$$\frac{d\mathbf{x}}{dt} = \mathbf{v}$$

$$\frac{d\mathbf{v}}{dt} = \frac{q_i}{m_i}\left(\mathbf{E} - \eta\delta\mathbf{J} + \mathbf{v}\times\mathbf{B}\right) \qquad (3)$$

$$\frac{dw}{dt} = -(1-w)\frac{d(\ln F_0)}{dt}$$

where $w = \delta F/F$ and F_0 is the equilibrium distribution function, taken to be a function of the particle integrals of motion $F_0 = F_0(\varepsilon, \lambda, p_\phi)$, where ε is the particle energy, $\lambda = \mu B_0/\varepsilon$ is the pitch-angle variable, $p_\phi = -\psi + Rv_\phi$ is the normalized toroidal angular momentum, and μ is an adiabatic invariant $\mu = \mu_0 + \mu_1$,[26] including first-order and some of the second-order corrections in ρ_i/L, where L is the equilibrium magnetic field scale length.

For the simulations presented in this paper, the equilibrium distribution function is taken to be of the form:[26] $F_0 = F_1(v)F_2(\lambda)F_3(p_\phi)$, where $v = \sqrt{2\varepsilon/m_i}$ is the particle velocity, and functions $F_{1,2,3}$ are defined by

$$F_1(v) = 1/(v^3 + v_*^3), \quad \text{for } v < v_0,$$

$$F_2(\lambda) = C\exp(-(\lambda - \lambda_0)^2/\Delta\lambda^2),$$

$$F_3(p_\phi) = \left[(p_\phi - p_{\min})/(p_{\max} - p_{\min})\right]^\alpha, \quad \text{for } p_\phi > p_{\min},$$

where $F_0 \to 0$ for $v > v_0$ or $p_\phi < p_{\min}$; v_0 is the injection velocity, and we assumed $v_* = v_0/2$. The parameters for the pitch-angle distribution are $\Delta\lambda = 0.3$ and $\lambda_0 = 0.7$. The function $F_3(p_\phi)$ is used to match the TRANSP profiles of the beam ion density, where $\alpha = 6$ is a numerical parameter, and the condition $p_\phi > p_{\min}$ describes a prompt-loss boundary, where $p_{\min} = -0.1\psi_0$ and $p_{\max} = R_0 v - \psi_0$ was assumed, R_0 is magnetic axis radius, and ψ_0 is value of poloidal flux on axis. A generalized form of the Grad–Shafranov equation solver has been developed, which includes, non-perturbatively, the effects of the beam ions with anisotropic distribution.[26] The beam ion beta in the NSTX can be relatively large, and the beam ion current density can be comparable to that of the thermal plasma. As a result, significant modifications of equilibrium occur due to self-consistent inclusion of the beam ions: more peaked current profile, anisotropic total pressure shifted relative to the flux surfaces, and increase in Shafranov shift—which all can have an indirect effect on stability properties.

III. SIMULATIONS OF SUB-CYCLOTRON FREQUENCY MODES FOR NSTX SHOT 141398

The excitation of CAEs has been studied for the H-mode plasma of NSTX shot 141398, and equilibrium profiles and plasma parameters have been chosen to match magnetic field and plasma profiles for this shot using the TRANSP code.[29] In the experiment, the plasma was heated by 6 MW of 90 keV Deuterium beams with $n_b = 3.5 \cdot 10^{18} m^{-3}$, $n_e = 6.7 \cdot 10^{19} m^{-3}$, $B_t = 0.325$ T, and $I_p = 0.8$ MA. For this particular shot, normalized beam ion injection velocity was high, $v_0 = 4.9 V_A$, due to a relatively low toroidal field, and as a consequence, significant GAE/CAE activity has been observed. Detailed measurements of GAE and CAE amplitudes and mode structures were obtained,[23,24] and the observed modes have been identified as
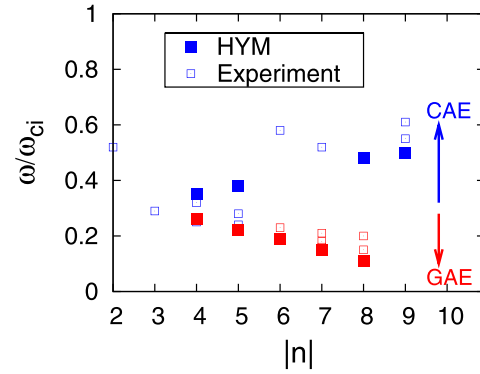
FIG. 1. Frequency versus toroidal mode number for unstable GAEs (red) and CAEs (blue), from HYM simulations and experimental data;[24,30] $f_{ci} = 2.5$ MHz.

counter-propagating CAE for frequencies $f > 600$ kHz, and small toroidal mode numbers $|n| < 6$, and as counter-propagating GAEs for $f < 600$ kHz, and $|n| \sim 6$–8 based on dispersion relations.[23,24] Co-propagating CAEs with higher toroidal mode numbers $n > 8$ have also been observed in the same shot.[30] Frequencies of the experimentally observed CAEs and GAEs[24,30] versus toroidal mode number are shown in Fig. 1 (open symbols), including a Doppler shift due to plasma rotation measured to be about $0.01\omega_{ci}$ near the magnetic axis. Figure 1 also summarizes the HYM simulation results. Numerical simulations show that most unstable modes for $n = 4$ and $n = 8, 9$ are co-rotating CAEs, which have been identified based on the calculated large compressional component of perturbed magnetic field in the core (Fig. 2(a)). The most unstable modes for $n = 5$–7 are counter-rotating GAEs, which have shear Alfvén wave polarization in the core with small $\delta B_\parallel$ (Fig. 2(b)). All unstable modes in simulations have small main poloidal mode numbers with $m \leq 3$. Calculated frequencies for $n = 5$–7 GAE are $\omega/\omega_{ci} = 0.15$–0.22 ($f = 380$–550 kHz), and higher frequencies for CAEs have been obtained with $\omega/\omega_{ci} = 0.35$–0.5 ($f = 870$–1200 kHz). Here all frequencies are given in plasma frame (no plasma rotation included in the numerical model), and normalized to the ion cyclotron frequency at the axis $f_{ci} = 2.5$ MHz.

The most unstable modes and, in some cases, second most unstable modes from the simulations are shown in Fig. 1 by solid symbols. The HYM code is an initial-value code; therefore, usually only the most unstable modes can be obtained in the linearized simulations for a given toroidal mode number. In some cases, a second most unstable mode can be found, if the two modes have comparable growth rates and different polarization (see Fig. 1 for $n = 4, 5$, and 8). Both experimental observations and numerical simulations demonstrate that for this particular shot a large number of GAEs and CAEs were excited by the beam ions. The calculated range of the unstable toroidal mode numbers, frequencies, and mode polarizations appears to be reasonably close to experimental observations.[23,24] Preliminary comparison of the radial structure of the GAEs shows a good agreement in the amplitude profiles, but differences in the phase profile plots.[31] One significant difference is that the unstable $n = 4$ CAE in simulations is co-rotating, whereas most experimentally observed
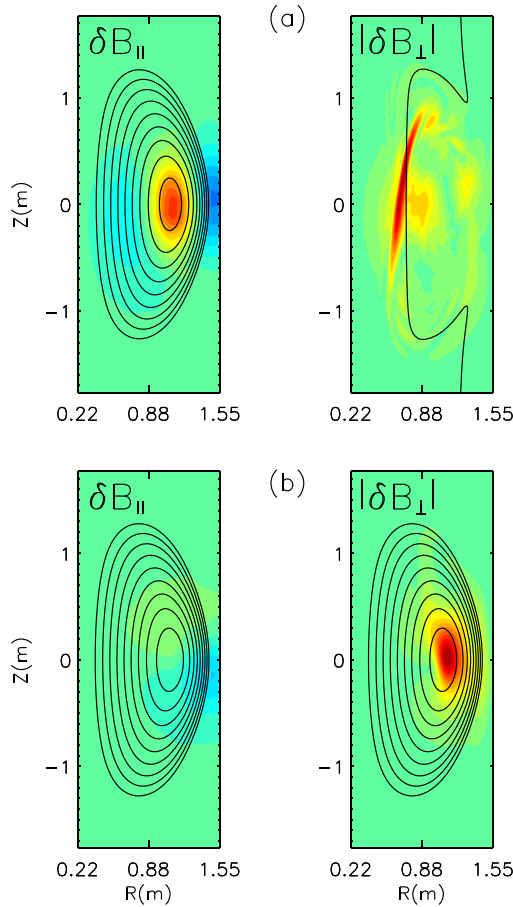
FIG. 2. Contour plots of magnetic field perturbation for (a) $n = 4$ co-rotating CAE and (b) $n = 6$ counter-rotating GAE. Also shown are poloidal flux contours and resonance contour $\omega_A(Z, R) = \omega$ for CAE. The CAE shows $\delta B_\parallel \gg \delta B_\perp$ in the core and a resonant coupling to KAW on HFS; for the $n = 6$ GAE, $\delta B_\parallel \ll \delta B_\perp$ in the core, but for both mode types $\delta B_\parallel \sim \delta B_\perp$ at the edge.

low-n CAEs are counter-rotating.[24] The reasons for these discrepancies are not understood, and will require further investigations. These could be related to the simplified form of the beam ion distribution functions used in the simulations or missing two-fluid effects and the bulk plasma rotation. It should be noted that some of the analytical calculations[32] also predict stronger instability of co-rotating CAEs, driven by the regular resonance with the beam ions, compared with the counter-rotating CAEs, driven by the Doppler-shifted cyclotron resonance. In addition, the simulations show that, at the low-field-side (LFS) plasma edge, both GAEs and CAEs have comparable amplitudes of compressional and perpendicular δB, which may contribute to the difficulty of correctly identifying these modes in the experiments based on the polarization data, especially for low n, when the two branches have similar frequencies $\sim 0.3\omega_{ci}$.

Both numerical and experimental data in Fig.1 demonstrate increase of the unstable CAE frequencies with toroidal mode number. This is consistent with reduction of the radial size of the effective potential well for CAE (described in Section IV) for higher $|n|$, and a related increase in $k_\perp \sim k_r$.[10] Unstable counter-rotating GAEs, on the other hand, exhibit a somewhat counter-intuitive decrease of frequency with $|n|$.

Simulations show that co- and counter-rotating AEs satisfy different resonant conditions, namely a regular resonance: $\omega = k_\parallel v_\parallel$ and the Doppler-shifted cyclotron resonance $\omega + k_\parallel v_\parallel \approx \langle \omega_{ci} \rangle$, respectively, where $v_\parallel$ and $\langle \omega_{ci} \rangle$ are the orbit-averaged parallel velocity and cyclotron frequency. For counter-GAEs, it follows that $\omega = \langle \omega_{ci} \rangle / (1 + v_\parallel / V_A)$, and the reduction of the most unstable ω implies that the resonance shifts well into the tail of the beam ion distribution. Thus, for the numerically calculated $n = 8$ counter-GAE: $\omega = 0.11\omega_{ci}$, and this resonant condition gives unreasonably large value of $v_\parallel / V_A = \langle \omega_{ci} \rangle / \omega - 1 \sim 7 > V_0 / V_A$ (where $\langle \omega_{ci} \rangle \sim 0.9\omega_{ci0}$, as calculated for resonant particles in simulations). This is resolved by retaining the particle drift frequency in the resonant condition, which can also be cast into the form $\langle \omega_d \rangle \approx s v_\parallel / (qR)$,[32] where $s = 0, \pm 1, \dots$ is integer, q is the safety factor, and R is the major radius, so that Doppler shift becomes $[k_\parallel + s/(qR)]v_\parallel$. The more accurate condition $v_\parallel / V_A = (\langle \omega_{ci} \rangle / \omega - 1)/(1 + sV_A/(qR\omega))$ then gives $v_\parallel / V_A < 5$ for $s \geq 3$.

IV. LINEAR SIMULATIONS

A. CAEs coupling to kinetic Alfvén wave

Figure 2(a) shows poloidal contour plots of the perturbed magnetic field for the $n = 4$ ($\omega = 0.35\omega_{ci}$) CAE. It can be seen that the CAEs are localized in the core, near the magnetic axis, where they have mostly compressional polarization, and $\delta B_\parallel$ is significantly larger than $\delta B_\perp$ everywhere, except in the radially localized region on the high-field-side (HFS) where the resonant condition $\omega_A(R, Z) = \omega$ is satisfied ($\omega_A(R, Z) = k_\parallel V_A(R, Z)$ is the local Alfvén frequency, and ω is the frequency of the CAE mode in the simulation). Simulations for both low-n and high-n co-rotating CAEs always show resonant coupling to the shear Alfvén wave. The amplitude of $\delta B_\perp$ at the resonance location is larger than the amplitude of the driving compressional mode (Fig. 3(a)). Analysis of magnetic and velocity perturbations of the resonant mode shows that its polarization is consistent with that of the kinetic Alfvén wave (KAW), namely that δB_Z and δV_Z are the dominant components, and $\delta V_Z \sim -\delta B_Z$. Figure 3 shows radial profiles of magnetic field and thermal pressure perturbations in the midplane. The resonant shear Alfvén perturbation can be seen at $R \sim 0.7$ m, in δB_R profile (green) and, most noticeably, in $\delta B_{R \times b}$ component of magnetic field
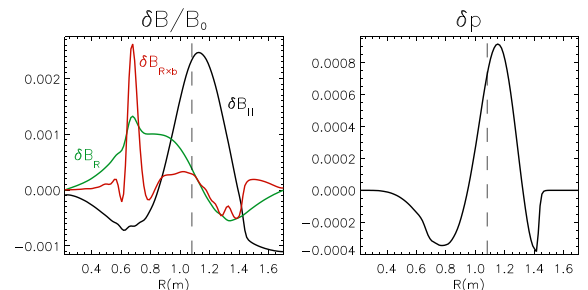
FIG. 3. Radial profiles of (a) magnetic field perturbation and (b) normalized thermal pressure perturbation (au) for the $n = 4$ CAE versus major radius. The CAE peaks near the magnetic axis $R = 1.07$ m.

(red). In contrast, the compressional component of $\delta\mathbf{B}$, the radial profile of perturbed pressure (Fig. 3(b)) and the radial profile of plasma density perturbation (not shown) all show a smooth behavior across the resonance, with very small short-scale resonant perturbations at $R \sim 0.7$ m. This demonstrates mostly incompressible nature of KAW. Note that the large-radial-scale structure of δB_R is related to the CAE.

The poloidal location of CAEs can be described by a simplified 2D wave equation using an effective potential[3,30]

$$\frac{\partial^2 \delta B_\parallel}{\partial r^2} = V_{eff}\delta B_\parallel, \quad \text{where } V_{eff} = -\omega^2/V_A^2 + k_\parallel^2.$$

The radial profiles of V_{eff} for the $n=8$ CAE mode with $\omega = 0.48\omega_{ci}$ (solid) and $n=4$ CAE with $\omega = 0.34\omega_{ci}$ (dashed) are shown in Fig. 4 for $k_\parallel = n/R(m=0)$. Compressional Alfvén waves can propagate for $V_{eff}<0$, but will be evanescent where $V_{eff}>0$. CAE can be described as a standing wave with radial extent of $V_{eff}<0$ which is 0.73 m $<R<$ 1.45 m for the $n=4$ mode, consistent with the mode structure shown in Figs. 2(a) and 3. Effective potential well for $n=8$ mode is narrower and deeper than V_{eff} for $n=4$ resulting in more localized CAE mode with larger frequency. Both modes have $m \approx 0$, and satisfy the fast wave dispersion relation with good accuracy.[33] Magnetic wells are shifted radially outwards relative to the magnetic axis location at $R = 1.07$ m. One of the notable features of CAEs is that the location of the shear Alfvén resonance always coincides with the edge of an effective potential within which the CAE is non-evanescent, because the condition $V_{eff}=0$ is identical to the Alfvén resonance condition (neglecting two-fluid effects and terms $\sim(\omega/\omega_{ci})^2$). This leads to a strong linear coupling between the compressional mode and the KAW. Resonance is more pronounced on the HFS, as can be seen, for example, from $\delta B_\perp$ plots in Fig. 3(a). As is shown below, this is related to the shape of the CAE potential well, which is relatively steep on the HFS, and has a very low wall at the LFS (Fig. 4), where $V_{eff} \approx -\omega^2/V_A^2 \sim n_i \approx 0$ near the plasma edge and further out.

In the ideal MHD model, there is a logarithmic singularity at the resonance location where the CAE frequency matches the local Alfvén frequency.[15] In the full kinetic model, this singularity is resolved by the thermal ion and fast ion FLR effects, and mode conversion to KAW. For the thermal plasma, neglecting the beam ion effects, the solution near the resonance can be expressed in terms of Airy and Scorer functions with an asymptotic form given by[15]
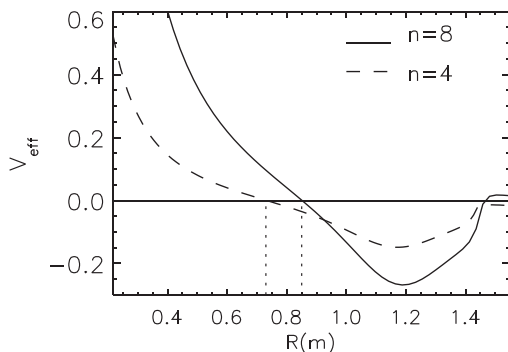
$$\delta E_R = -\pi\left(\frac{L}{\rho}\right)^{2/3} E_0\left[i\text{Ai}\left(-\frac{x}{\Delta}\right) + \text{Gi}\left(-\frac{x}{\Delta}\right)\right]$$

$$\approx -E_0\sqrt{\pi}\left(\frac{L}{\rho}\right)^{2/3}\left(\frac{\Delta}{x}\right)^{1/4}\exp\left[i\left(\frac{2}{3}\left(\frac{x}{\Delta}\right)^{3/2} + \frac{\pi}{4}\right)\right]$$

$$+ E_0\frac{L}{x}, \tag{4}$$

where for our application L is a characteristic radial scale length of $V_A(R)$, $x = R - R_{res}$, R_{res} is the resonance location, E_0 is the amplitude of the CAE at the resonance, $\Delta = (L\rho^2)^{1/3}$, $\rho^2 = (3/4 + T_e/T_i)\rho_i^2$, and ρ_i is the thermal ion Larmor radius. In a three component plasma including the thermal ions, electrons, and the beam ions, the expression for the effective Larmor radius becomes[14]

$$\rho^2 = \left(\frac{3}{4}\frac{n_i}{n_e} + \frac{3}{4}\frac{n_b}{n_e}\frac{T_b}{T_i} + \frac{T_e}{T_i}\right)\rho_i^2 = \left(\frac{3}{4}\left[1 + \frac{\beta_b}{\beta_i}\right] + \frac{\beta_e}{\beta_i}\right)\frac{n_i}{n_e}\rho_i^2, \tag{5}$$

where β_b and β_i are the beam and thermal ion beta, respectively. As can be seen from Eq. (4), the effective wave number of KAW near the resonance is $k_\perp \sim 1/\Delta = (L\rho^2)^{-1/3}$, and further away from the resonance it increases to $k_\perp \sim 1/\rho$. From TRANSP data for this shot we have $\beta_b = 0.12$ and $\beta_i = 0.09$, $T_e/T_i = 0.88$, and the effective beam ion temperature calculated from $\beta_b/\beta_i = 1.33$ is $T_b/T_i = 25.2$. The magnitude of the equilibrium magnetic field at the HFS resonance is $B \sim 1.5B_0 = 0.49$ T, and the local thermal ion, beam ion, and effective Larmor radius from Eq. (5) can be calculated as $\rho_i = 0.9$ cm, $\rho_b = 4.4$ cm, and $\rho = 1.5$ cm, respectively. At the midplane ($z=0$) the KAW-related magnetic perturbation is $\delta B_Z = n\delta E_R/(\omega R) \sim -Gi(-x/\Delta)$, where the distance between first two maximums of the Scorer function $Gi(\xi)$ is ≈ 4.7.[34] The radial scale of KAW at the resonance defined as 4.7Δ, therefore, can be estimated as $\Delta R = 4.7(L\rho^2)^{1/3} \sim 21$ cm, assuming $L \sim 40$ cm on HFS.

The HYM numerical model treats the thermal plasma as an MHD fluid, and the KAW perpendicular scale in the simulations is determined only by the beam ion FLR effects. Neglecting thermal plasma FLR effects in Eq. (5), we get $\rho = \sqrt{3/4(n_b/n_e)}\rho_b \sim 1$ cm. The radial scale of KAW in this model is $\Delta R = 4.7(L\rho^2)^{1/3} \sim 16$ cm, which agrees reasonably well with the simulation results where $\Delta R \sim 15 - 20$ cm (Fig. 3(a)). However, it should be noted that Eqs. (4) and (5) were derived assuming that $k_\perp\rho_b \ll 1$, whereas for the simulation parameters, $k_\perp\rho_b \sim 1.4 > 1$, and more accurate calculations including a full Bessel function without the expansion would be needed for a proper comparison. Since the HYM does not include thermal ion FLR effects, it underestimates the KAW radial scale length; however, the CAE/KAW coupling in this model is qualitatively correct, as follows from the local dispersion relation.[14]

The CAE potential well (Fig. 4) is shifted radially outwards relative to magnetic axis, and it is not symmetric. The

FIG. 4. Radial profiles of the effective potential V_{eff} for the $n=8$ CAE with $\omega = 0.48\omega_{ci0}$ (solid) and $n=4$ CAE with $\omega = 0.34\omega_{ci0}$ (dashed). The potential well corresponds to $V_{eff}<0$.
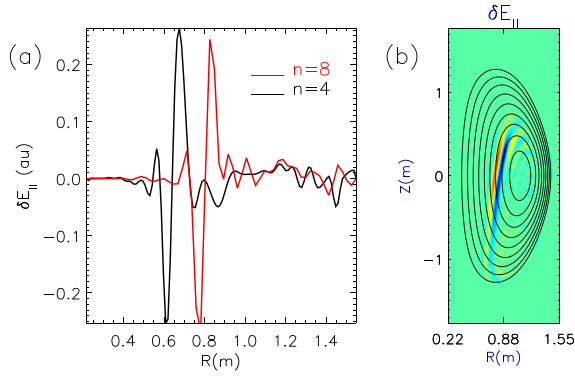
FIG. 5. (a) Radial profiles of $\delta E_\parallel$ from CAE/KAW simulations for $n=4$ (black) and $n=8$ (red); (b) contour plot of $\delta E_\parallel$ for the $n=8$ CAE/KAW.

low field side near the edge has a much flatter $V_A(R)$ profile compared with the HFS, and a very shallow "potential wall," which means that the characteristic scale length L becomes too large for the assumptions used to obtain the KAW solution[15] to be valid. Thus, the KAW radial scale, estimated as above, becomes larger than that of the background plasma. In simulations, this is manifested as a lack of sharp resonance structures on the LFS even for the higher-n CAEs. Also, since the KAW is mostly an incompressible mode, the plasma pressure and density perturbations associated with the KAW are very small, as can be seen in Fig. 3, which does not show any small scale resonant structures in the radial perturbed pressure profile at $R \sim 0.7$ m.

The condition $k_\perp \rho_b \sim 1$ implies that the beam ion and electron motions are decoupled in KAW, leading to generation of finite parallel electric field perturbations, which is typical for KAW. Figure 5 shows the radial profiles and poloidal contour plot of $\delta E_\parallel$ obtained in simulations of the $n=4$ and $n=8$ CAE/KAW instabilities. It is seen that the $\delta E_\parallel$ location and poloidal structure are related to the KAW, whereas the CAE has an ideal MHD character with negligible $\delta E_\parallel$. Finite $\delta E_\parallel$ is important for effective dissipation of the wave energy at the resonance location, and electron heating via Landau damping. In addition, radially overlapping KAWs can strongly enhance plasma heat transport due to finite $\delta E_\parallel$. Previous studies have shown that addition of the finite parallel electric field to ideal GAE structure has a strong effect on the electron transport.[12] Our simulations show that the radial width of KAWs is relatively large on the HFS in NSTX. Therefore, in cases when several CAEs are observed, the KAWs will overlap radially. For example, for the $n=8$ and $n=4$ CAEs considered here with resonances located at $R=0.73$ m and $R=0.85$ m, respectively, the KAWs overlap significantly as can be seen from radial profiles of $\delta E_\parallel$ in Fig. 5(a). Therefore, in addition to the energy channelling mechanism, discussed in Sec. V, several overlapping KAWs with relatively large $\delta E_\parallel$ can also have a direct effect on both the electron transport and the beam ion re-distribution.

B. Resonant excitation of CAEs by the beam ions

In NSTX, the CAEs are driven unstable by the resonant interaction with the beam ions. The delta-f method used in

the HYM code permits a simple numerical criterion for resonant particles. Thus, we label a simulation particle as a resonant whenever its weight is significantly larger than the average weight. Specifically, the condition $|w| > 0.15 w_{max}$ has been used in most cases.

In the simulations the orbit-averaged cyclotron frequency, toroidal and poloidal frequencies, and the averaged parallel velocity have been calculated for each particle. Several examples of the resonant particle plots obtained in linearized simulations of the $n=8$ CAE with $\omega = 0.48 \omega_{ci}$ are shown in Figs. 6 and 7 and discussed in detail in this subsection.

The general resonance condition can be written as $\omega - n\omega_{tor} - k\omega_{pol} = l\omega_{ci}$, where ω_{tor} and ω_{pol} are toroidal and poloidal orbit frequencies, k is an integer, and $l = 0, \pm 1$. Numerical analysis of the resonant wave-particle interaction for the $n=8$ CAE simulation (Fig. 6(a)) shows two separate
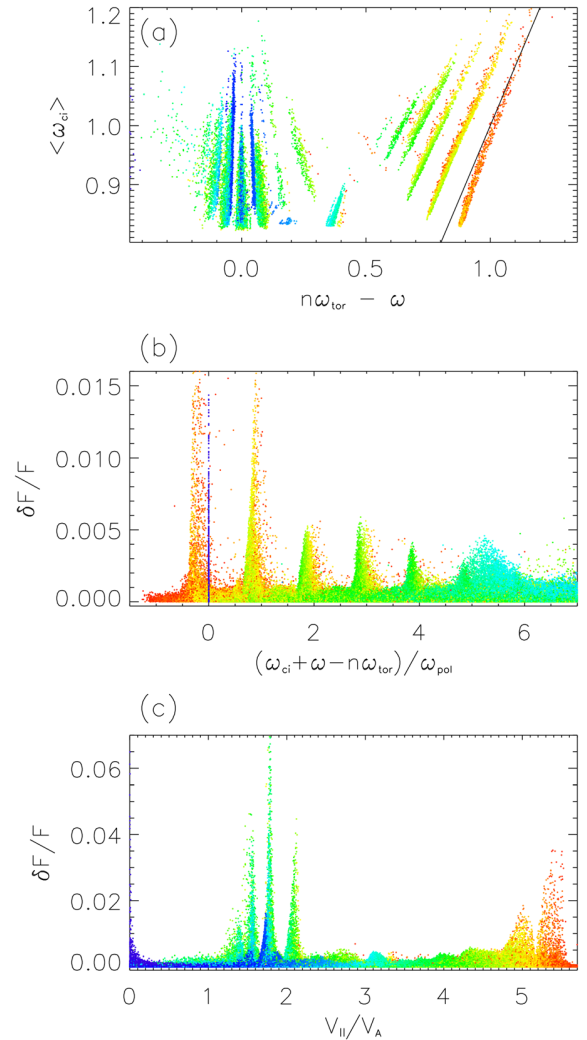
FIG. 6. (a) Scatter plot showing orbit-averaged cyclotron and toroidal frequencies of resonant particles normalized to the ion cyclotron frequency at the axis, ω_{ci0}; (b) Particle weight $w \sim \delta F/F$ vs cyclotron resonance condition: $\omega + \omega_{ci} - n\omega_{tor} - k\omega_{pol} = 0$ for all particles, k is integer; (c) particle weight vs orbit-averaged parallel velocity for all particles. From HYM simulations of the $n=8$ co-rotating CAE with $\omega = 0.48 \omega_{ci}$. Particle colour corresponds to different energies: from $\varepsilon = 0$ (purple) to $\varepsilon = 90$ keV (red) with colour scale shown in Fig. 7(a).
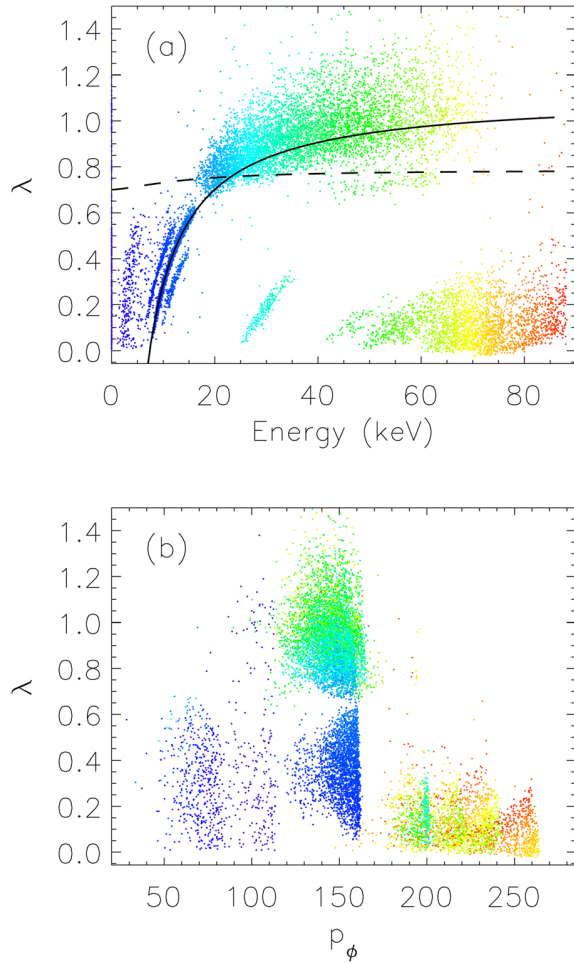
FIG. 7. Location of resonant particles in phase space, (a) $\lambda = \mu B_0/\varepsilon$ vs energy, and (b) λ vs toroidal angular momentum $p_\phi = Rv_\phi - \psi$; from simulations of the $n = 8$ CAE. Solid line approximately corresponds to $v_\parallel = 1.7V_A$ condition, and dashed line represents condition: $\frac{\partial F_0}{\partial \varepsilon} - \frac{\lambda}{\varepsilon}\frac{\partial F_0}{\partial \lambda} = 0$. Particle colour corresponds to different energies: from $\varepsilon = 0$ (purple) to 90 keV (red).

groups of resonant particles, one group which satisfies the regular ($l = 0$) resonance condition: $\omega - k_\parallel v_\parallel = 0$ (or approximately, $\omega - n\omega_{tor} = 0$), and a group of higher energy particles which satisfy the Doppler-shifted cyclotron resonant condition: $\omega + \omega_{ci} = k_\parallel v_\parallel$ with $l = -1$ (solid line in Fig. 6(a) corresponds to the cyclotron resonance $\omega + \omega_{ci} = n\omega_{tor}$). Poloidal frequency is small compared with other frequencies, $\omega_{pol} \sim 0.08\omega_{ci0}$, resulting in the fine splitting of resonances, as can be seen in Fig. 6(b), where the weights of all simulations particles are plotted vs $k = (\omega_{ci} + \omega - n\omega_{tor})/\omega_{pol}$ (all frequencies are orbit averaged). Cyclotron resonances correspond to integer values of the abscissa, as can be seen by the peaks of $\delta F/F$, whereas lower energy particles which satisfy $\omega - n\omega_{tor} \approx 0$ are out of k range in this plot. Note that in order for a co-rotating CAE to satisfy the cyclotron resonance condition, the Doppler shift has to be larger than the cyclotron frequency, which can be a case for the large-n CAEs. Lower-n CAEs, in particular the $n = 4$ CAE, show resonant interaction only for the main $l = 0$ resonance.

There is a third group of large-weight particles seen in Fig. 6 in light blue colour. A separate simulation with

suppressed CAE has shown that these particles are in $l = 1$ resonance with counter-rotating GAE mode, with $\omega = 0.11\omega_{ci}$, which was also unstable in the $n = 8$ linearized simulation. These particles have $\langle\omega_{ci}\rangle \sim 0.85$, and $n\omega_{tor} - \omega \approx 0.35$ in Fig. 6(a); they can be seen as large-weight particles for $k \sim 4.5$–6 in Fig. 6(b), and do not satisfy $l = -1$ cyclotron resonance condition.

Figure 6(c) shows distribution of particle weights versus orbit-averaged $v_\parallel/V_A$ values, and particle colour corresponds to different energies: from $\varepsilon = 0$ (purple) to $\varepsilon = 90$ keV (red), where the colour coding could be seen in Fig. 7(a). Large-weight (resonant) particles which satisfy regular ($l = 0$) resonance condition with CAE have $v_\parallel/V_A \sim 1.5$–2.0; the $l = -1$ cyclotron resonant condition is satisfied for particles mostly from the tail with $v_\parallel \sim V_0 \approx 5V_A$; and a group of particles resonant with the counter-GAE have $v_\parallel/V_A \sim 3$. It has been found that the main contribution to the CAE instability drive comes from the regular resonance, i.e., from the beam ions with parallel velocity comparable to the phase velocity of the CAE: $v_\parallel \sim \omega/k_\parallel$. This was verified by a separate simulation, where the contribution of the high-energy cyclotron-resonant particles was "turned off" by setting their weights to zero, resulting in no significant changes in the growth rate of CAE. For the $n = 8$ mode with $\omega = 0.48\omega_{ci}$, the resonant velocity can be estimated as $v_\parallel \approx \omega R_0/n = 1.7V_A$, in good agreement with the simulation results in Fig. 6(c).

Figure 7 shows the location of the resonant particles in the phase space $(\varepsilon, \lambda, p_\phi)$, where $p_\phi = -\psi + (m_ic/q_i)Rv_\phi$ is the toroidal angular momentum normalized in the code units (normalized by $B_0d_i^2$, where $d_i = 3.93$ cm is the ion skin depth at the axis; the normalized flux is $\psi_0 = -110$ at the axis, and $\psi = 0$ at the edge). With the exception of the light-blue group of particles which are resonant with counter-GAE ($\varepsilon \sim 25$–35 keV, $\lambda < 0.4$, and $p_\phi \sim 200$), two types of particles resonant with the $n = 8$ CAE can be seen. Largest effect on the CAE instability ($l = 0$ resonance) have lower-energy particles which have wide range of pitch-angle parameter $\lambda = 0.1$–1.2 and energies $\varepsilon = 10$–60 keV, with $p_\phi \sim 130$–160. At the same time, these particles have a relatively narrow range of $v_\parallel$, and their distribution in (λ, ε) space can be described approximately by a relation $\lambda = B_0/\langle B \rangle(1 - m_iv_\parallel^2/2\varepsilon)$ for a fixed $v_\parallel$, which is plotted by a solid line in Fig. 7(a) for $v_\parallel = 1.7V_A$ and $\langle B \rangle/B_0 = 0.9$. Wider spread from this line at large λ is related to larger FLR corrections to μ.[26] This group includes both passing and trapped particles. The high-energy group ($l = -1$ resonance) are passing particles with $\varepsilon \gtrsim 65$ keV, low λ ($\lambda < 0.4$), and $p_\phi \sim 170$–265. Sharp boundaries in p_ϕ plot in Fig. 7(b) indicate that low-λ resonant particles are located close to the boundary $p_\phi \leq p_{max}$ in the phase-space, where values $p_\phi = p_{max} = -\psi_0 + R_0v\sqrt{1 - \lambda}$ correspond to orbits passing through the magnetic axis.

Linear theories of the beam-driven CAE instability have been developed in Refs. 3 and 32. Only counter-CAEs driven by the $l = 1$ resonance have been considered in Ref. 3, and the instability condition $1 < k_\perp\rho_b < 2$ has been obtained, where $k_\perp$ is a perpendicular wave number for the CAE. It has been suggested that the main instability drive comes from the trapped beam ions. Both co- and counter-CAEs

have been studied in Ref. 32, and it has been shown that co-CAE driven by $l = 0$ resonance are unstable for a wider range of the beam ion parameters, i.e., $0 < k_\perp \rho_b \leq 2$, but this calculation considered only the circulating particles. Both calculations assumed no p_ϕ dependence in F_0, and delta-function distribution in λ, $F_0 = F_0(\varepsilon, \lambda) \sim \delta(\lambda - \lambda_0)$. For comparison, our calculations show that the particles satisfying the $l = 0$ resonance condition in simulations of the $n = 8$ co-CAE have range of $k_\perp \rho_b$ values from ~ 0.7 for colder beam ions to $k_\perp \rho_b \sim 2.1$ for the particles with energies ~ 50 keV. The gaps in λ distribution around $\lambda_0 = 0.7$ seen in Fig. 7 show that there are no resonant particles in the simulation with large weights near $\lambda \sim \lambda_0$, where $\partial F_0/\partial \lambda = 0$. This indicates that in the weight evolution equation of the delta-f scheme Eq. (3), the term proportional to $\partial(\ln F_0)/\partial \lambda$ makes the largest contribution to $d(\ln F_0)/dt$, at least for the resonant particles. The dashed line plotted in Fig. 7(a) shows a condition: $D = \partial F_0/\partial \varepsilon - (\lambda/\varepsilon)\partial F_0/\partial \lambda = 0$, where $D > 0$ above the dashed line and $D < 0$ below it. Assuming that the growth rate of co-CAE is approximately proportional to D,[32] the regions of the (ε, λ) phase-space above this line are responsible for the instability, and therefore, in the simulation the instability is driven mostly by the trapped beam ions, whereas lower-energy passing ions are stabilizing. Note that the above expression for D applies only for the $l = 0$ resonance.

The resonant particle plots similar to Figs. 6 and 7 have also been obtained for the $n = 4$ co-rotating CAE, except that in case of $n = 4$ CAE, there were no particles satisfying the $l = -1$ cyclotron resonance condition due to smaller value of $k_\parallel$ and a smaller Doppler shift. Linear simulations also show that both low-n and high-n unstable CAEs have low poloidal mode numbers $m = 0$–2, and their poloidal mode extent overlaps significantly with the beam ion orbits, indicating a very effective resonant interaction.

V. NONLINEAR SIMULATIONS OF $n = 4$ co-CAE

Nonlinear simulations of the $n = 4$ CAE have been performed for the beam ion parameters corresponding to NSTX shot 141398. These simulations have been carried out in order to identify the CAE saturation mechanism, find the mode amplitude at the saturation and compare with experimental data, and calculate self-consistently the fraction of the beam power going into the excitation of a CAE, and being channeled to KAW and absorbed at the resonance. The simulations are fully nonlinear including 32 toroidal harmonics, and show saturation of the $n = 4$ CAE mode. Initial conditions for the nonlinear run were obtained by running the $n = 4$ linearized simulations ($t\omega_{ci} = 0$–600, Fig. 8) to obtain a converged linear mode structure of the CAE. The nonlinear run starts at $t\omega_{ci} = 600$, and also shows growth of the $n = 5$, 6, 7 GAEs and $n = 8$ CAE modes. The $n = 6$ and 7 GAEs have larger linear growth rates than the $n = 4$ CAE mode, and saturate at higher amplitudes as seen in Fig. 8. The timing of the switch between the $n = 4$ linearized run and the fully nonlinear run was chosen in such a way, as to allow the $n = 4$ CAE saturate ($t\omega_{ci} \sim 750$) while the amplitudes of other unstable modes were still relatively small. This
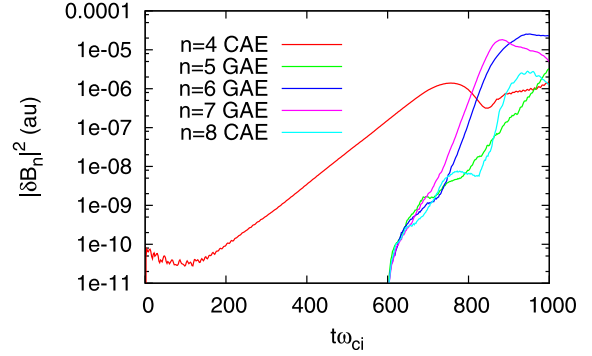
FIG. 8. Time evolution of volume-averaged amplitudes of different toroidal harmonics of the perturbed magnetic field from simulations of $n = 4$ CAE. Fully nonlinear simulations start at $t\omega_{ci} = 600$.

allowed a calculation of the fraction of the beam power taken by the $n = 4$ CAE and the energy flux from the single CAE to KAW near the saturation.

In the simulations, the unstable $n = 4$ mode ($\omega = 0.34\omega_{ci}$, and $\gamma = 0.01\omega_{ci}$) has been identified as a co-rotating CAE based on a dominant parallel component of the perturbed magnetic field in the core; however, significant perpendicular component $|\delta B_\perp| \sim |\delta B_\parallel|$ has been found at the plasma edge on the LFS for this mode. Figure 9 shows the time evolution of $\delta B_\parallel$ and two components of $\delta \mathbf{B}_\perp$ at the core, and close to the plasma edge in the equatorial plane from the same nonlinear simulations of the $n = 4$ CAE as in Fig. 8. It is seen that in the core, the compressional perturbation is 3–4 times larger than the $|\delta B_\perp|$ till $t\omega_{ci} < 800$, at which point the higher-n GAE perturbations grow to large amplitude (Fig. 9(a)). It is interesting
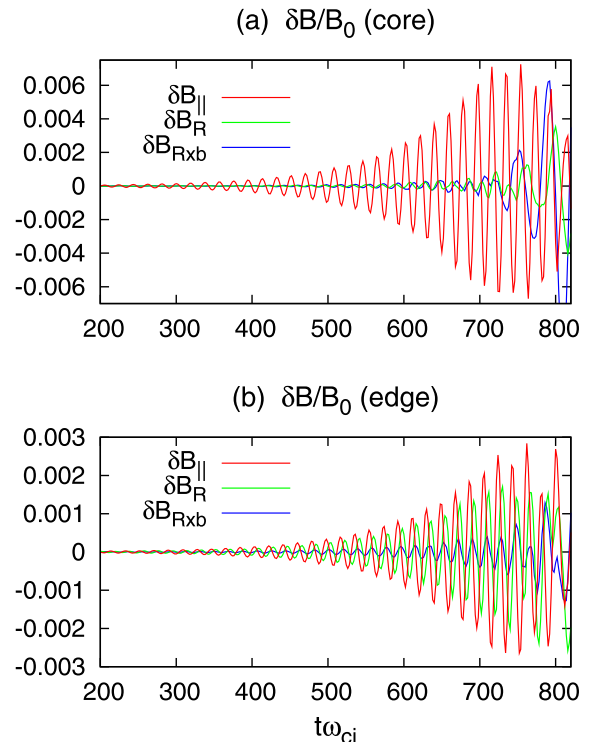
FIG. 9. Time evolution of $\delta B_\parallel$ and two components of $\delta \mathbf{B}_\perp$ at the core, and close to the plasma edge in the equatorial plane on LFS. From nonlinear simulations of the $n = 4$ CAE.
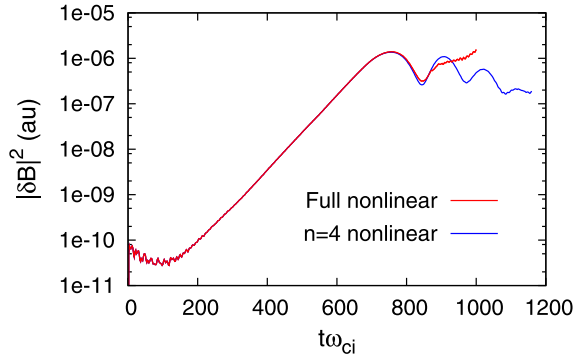
FIG. 10. Time evolution of $n=4$ CAE amplitude from fully nonlinear simulations (red), and from a nonlinear simulation including only the $n=4$ harmonic (blue).

that the mixed compressional/shear polarization near the plasma edge on the LFS was also obtained in simulations of the GAEs,[27] where the magnetic perturbations have shear Alfvén wave polarization in the core with dominant $\delta\mathbf{B}_\perp$; however, they also have a significant compressional component at the edge. Strong coupling between shear Alfvén and compressional perturbations in the NSTX simulations is related to small aspect-ratio, relatively high beta and kinetic effects due to energetic particles. Thermal plasma two-fluid effects, which are not included in HYM version used here, will also contribute to coupling. Experimental magnetic measurements at the edge also show the mixed compressional/shear Alfvén polarization for both CAEs and GAEs in NSTX.[30,35]

The saturation amplitude of the $n=4$ CAE instability in the simulations is $\delta B_\parallel/B_0 = 6.6 \times 10^{-3}$, which is larger than the values obtained by analysing experimental data from the same NSTX shot. Thus, measured plasma displacements $|\xi| = 0.1$–0.4 mm of unstable CAEs[24] correspond to magnetic perturbations in the range $\delta B_\parallel/B_0 = (0.9$–$3.4) \times 10^{-3}$, where we have used the HYM-calculated mode structure to relate displacement and magnetic field perturbation amplitudes. More recent analysis of experimental data[31,36] suggests even smaller values $\delta B_\parallel/B_0 = (0.2$–$0.7) \times 10^{-3}$. In the simulations the instability saturates due to nonlinear particle trapping, which has been confirmed by scaling of the saturation amplitude with the growth rate $\delta B_\parallel \sim \gamma^2$, as reported in Sec. VI, and it has been verified in a separate nonlinear simulation including only the $n=4$ toroidal harmonic. Figure 10 shows a comparison of time evolutions of the $n=4$ CAE amplitude from the fully 3D nonlinear and single harmonic nonlinear simulations. The saturation amplitude is identical in both cases, indicating that the instability saturates mainly through the changes in the beam ion distribution function, and field nonlinearities play a minor role. The frequency of nonlinear oscillations in Fig. 10 is $\omega_{bounce} \sim 0.04\omega_{ci}$, which is comparable with linear drive $\gamma_{drive} \approx 0.03\omega_{ci}$, calculated in Sec. VI, which is also consistent with the particle trapping saturation mechanism.

Convergence of the nonlinear results has been verified by running nonlinear simulations with higher grid resolution, and changing the number of simulation particles from 2 M to 20 M - no significant changes have been observed in linear growth rate or saturation amplitude of the $n=4$ CAE. Another indication of sufficient resolution in the simulations
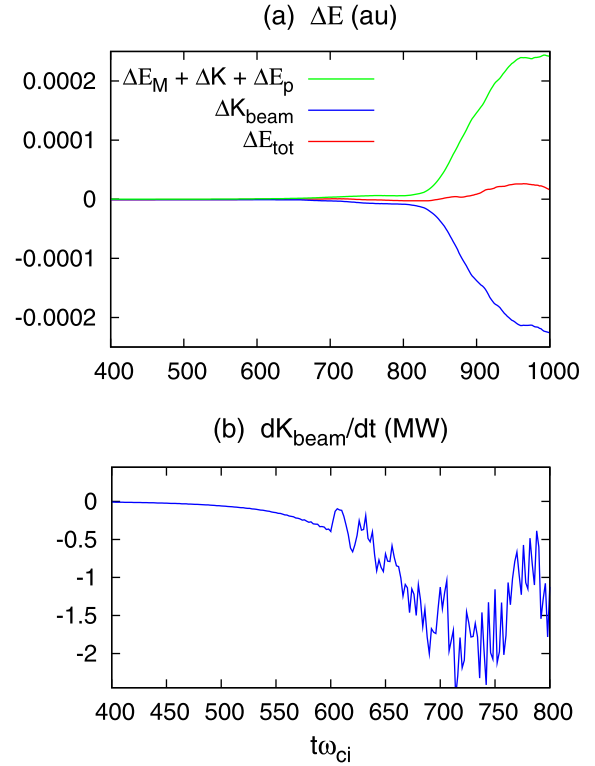
FIG. 11. (a) Time evolution of change in bulk fluid energy (green), the beam ion energy (blue), and the total energy of the system (red); (b) Time evolution of rate of change of beam ion energy, calculated as $\int(\mathbf{J}_{beam}\cdot\mathbf{E})d^3x$.

is a good conservation of the total energy, as shown in Fig. 11, where the relative change in the total energy vs change in the beam ion kinetic energy is about 4% at $t < 880(1/\omega_{ci})$, and less than 12% overall. Here the bulk fluid energy (i.e., magnetic field plus thermal plasma energy) was calculated as $E_{MHD} = \int[B^2/8\pi + p/(\gamma-1) + \rho v^2/2]d^3\mathbf{x}$.

Figure 11(b) shows that the rate of change of the beam ion energy, calculated as $dK_{beam}/dt = \int(\mathbf{J}_{beam}\cdot\mathbf{E})d^3x$, can be as large as ~ 1.5 MW near the $n=4$ CAE saturation at $t \sim 750(1/\omega_{ci})$, demonstrating that a significant fraction of the total beam power can be transferred to a single CAE of relatively large amplitude. Note that this estimate reduces to ~ 0.4 MW, if scaled to experimentally relevant amplitudes $\delta B/B_0 = 3.4 \times 10^{-3}$.[14]

Energy flux from unstable CAE to KAW location can be calculated as $\mathbf{S} = \mathbf{E} \times \mathbf{B}/4\pi + p\mathbf{V}\gamma/(\gamma-1)$, where the bulk plasma kinetic energy flux can be neglected as being a third-order in the perturbation amplitude. Calculations show that the pressure related term has the same sign as the Poynting flux, but it is about 14% of the total flux, proportional to plasma beta.

Plots of the normal energy flux $\mathbf{S}_\psi = (\mathbf{S}\cdot\mathbf{n})\mathbf{n}$ (where $\mathbf{n} = \nabla\psi/|\nabla\psi|$) in the poloidal plane (Fig. 12) shows that the energy flux is mostly directed radially away from the magnetic axis and towards the HFS resonance with KAW. There is a significant drop in S_ψ at the KAW location, indicating the power absorption. Calculated change of the energy flux across the resonant layer at $R = 0.6$–0.7 m at time $t = 750(1/\omega_{ci})$, corresponding to the peak of the CAE amplitude, is 3×10^5 W/m^2. Calculating the surface integral over the whole
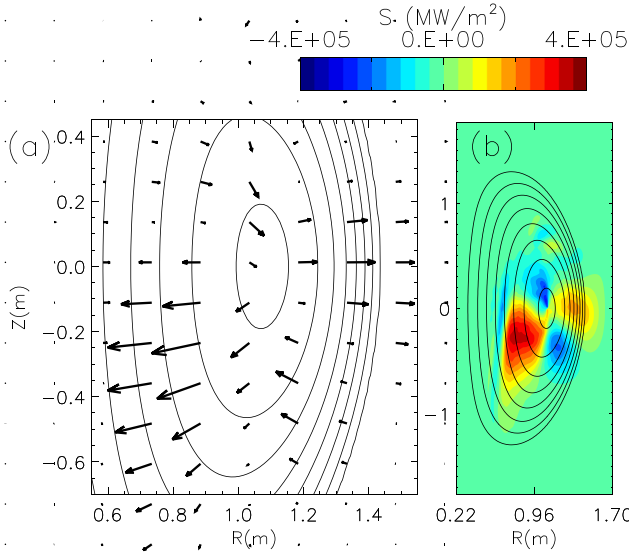
FIG. 12. (a) Vector plot of the energy flux $\mathbf{S}_\psi$; (b) contour plot of the normal component of S_ψ in poloidal plane from nonlinear simulations of the $n = 4$ CAE/KAW at $t = 750(1/\omega_{ci})$.

Z range at each R as $P = (2\pi R)\int S_R dz$, the power absorption at $R = 0.7$ m can be calculated as $P \sim 1.2$ MW. This value is overestimated, because the numerically obtained saturation amplitude of the CAE is larger than the observed amplitudes. When scaled down to $\delta B/B_0 = 3.4 \times 10^{-3}$, the estimated power absorption becomes ~ 0.3 MW, proportional to the square of the local CAE amplitude.[21] In the case of smaller observed magnetic perturbations of $\delta B/B_0 \sim 1 \times 10^{-3}$ [31,36] at least 4 unstable CAEs will be needed for ~ 0.1 MW power absorption at the resonance. In either case, the nonlinear simulations demonstrate that a significant fraction of the total beam power can go into the excitation of a single CAE, and then be channeled by the CAE to the resonance location at the edge of the beam, and absorbed there. Considering a large number of unstable CAEs observed experimentally in this particular NSTX shot,[24] the total power channeled to the KAWs can significantly affect the beam energy deposition profile, and lead to electron heating closer to the edge. The HYM thermal plasma model includes viscous damping and Ohmic dissipation of $\delta J_\parallel$. In collisionless plasma, the energy can be dissipated at the resonance location via the electron Landau damping,[15] resulting in increased electron temperature near the edge, and flattening of the electron temperature profile. The nearly field-aligned structure of the KAW with finite $\delta E_\parallel$ (Fig. 5) will result in a strong interaction with resonant electrons, and heating.

VI. SCALING WITH BEAM POWER

An additional set of linearized and nonlinear simulations have been performed for the $n = 4$ CAE instability for varying the beam ion density. The results of these simulations, namely the scaling of the instability growth rate, saturation amplitude, and mode-converted power, are summarized in Fig. 13.
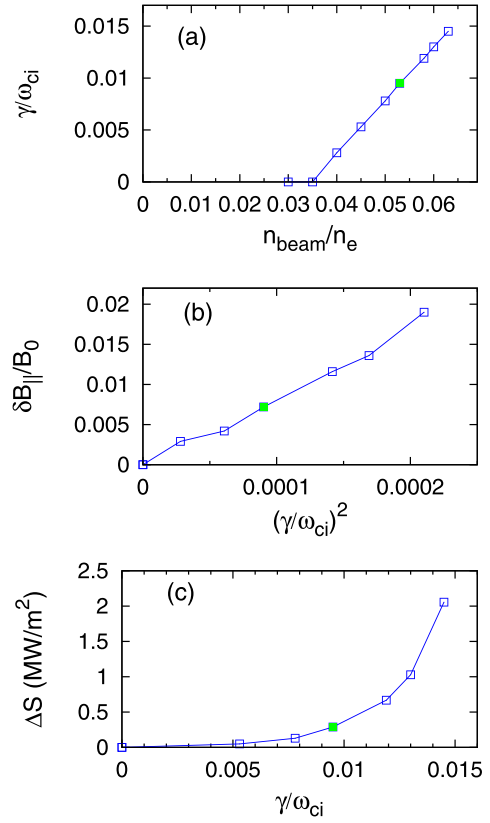
FIG. 13. (a) Dependence of linear growth rate of the $n = 4$ CAE on the beam ion density; (b) Saturation amplitude of CAEs vs square of the linear growth rate; (c) Calculated change of the energy flux at the resonance location near the instability saturation vs the normalized growth rate. Solid symbols (green) correspond to the experimental conditions for NSTX shot # 141398.

Simulations have been performed for fixed beam ion distribution function and thermal plasma parameters, except that the peak beam ion density has been varied from $0.03 n_e$ to $0.063 n_e$. A new self-consistent equilibrium has been calculated for each case. Figure 13(a) shows that the growth rate of the $n = 4$ CAE scales linearly with beam ion density, and there is a threshold of $n_b \leq 0.035 n_e$, below which the mode is stable. The parameters for the NSTX shot # 141398 correspond to $n_{b0} = 0.053 n_e$ and $\gamma = 0.0095 \omega_{ci}$. Assuming that the instability drive is proportional to the beam ion density and using $0.035 n_e$ as threshold density, we can estimate the drive and damping rates from $\gamma = \gamma_{dr0}(n_b/n_{b0}) - \gamma_{damp}$, where $\gamma_{damp} = 0.0185 \omega_{ci}$ is the CAE damping rate due to coupling to KAW, and $\gamma_{dr0} = 0.028 \omega_{ci}$ is the beam ion drive for the experimental value of the beam density $n_{b0} = 0.053 n_e$. Due to strong linear CAE/KAW coupling, the damping rate is large $\gamma_{damp} = 0.66 \gamma_{dr0}$. The beam power for the NSTX shot # 141398 was $P = 6$ MW; therefore, the threshold value of the beam power needed for the excitation of the $n = 4$ CAE can be estimated as $P \sim 4$ MW. This estimate is consistent with experimental results showing a large number of unstable sub-cyclotron frequency Alfvén modes when the beam power is sufficiently large $P \geq 4$ MW.[1] Damping rates of higher-n CAEs due to coupling to KAW are expected to be higher than that for small n, because of a smaller radial extent of the

large-n CAE effective potential well, and localization of the resonances at smaller minor radii, where the plasma density is higher and absorption is stronger.[21]

Fully nonlinear simulations, similar to those described in Sec. V have been carried out for each value of beam ion density, and show that the saturation amplitude of the $n = 4$ CAE scales approximately as square of the growth rate, i.e., $|\delta B_\parallel / B_0| \sim (\gamma / \omega_{ci})^2$ (Fig. 13(b)), consistent with the particle trapping saturation mechanism. Analysis of the experimental data from the database of the NSTX shots[37] shows somewhat stronger than quadratic scaling of the GAEs and CAEs amplitudes with beam power; i.e., it gives $|\delta B / B_0| \sim P^{2.6}$.[38] The difference with simulation results could be related to separation of the single unstable mode in the nonlinear simulations, or, possibly, due to the amplitude-weighted averaging done in the data analysis.

Absorption rate, calculated as a change in the Poynting flux across the resonance layer, has been obtained in each simulation, and it shows a very strong scaling with growth rate/beam power (Fig. 13(c)). The best fit with the power law gives $\Delta S \sim (\gamma / \omega_{ci})^5$, implying that the energy loss at the resonance scales as the fifth power of the beam ion density (or the beam power). The strong scaling could be explained, if one assumes that the power absorbed at the resonance is proportional to the change in the CAE energy $P = 2\gamma \int (\delta B)^2 / 4\pi \, d^3x \sim \gamma^5$. These results suggest that the energy channelling mechanism might play a significant role in the NSTX-U due to higher projected beam powers, provided that the CAEs are still unstable for larger toroidal field values (i.e., smaller values of v_0 / V_A parameter).

VII. SUMMARY

Numerical simulations presented here demonstrate that the beam-driven CAEs are strongly coupled with kinetic Alfvén waves at the Alfvén resonance location in NSTX. The resonant mode conversion of CAE to KAW occurs for any unstable CAE, independent of toroidal mode number or mode frequency, and it follows from dispersion relation. The strong linear CAE/KAW coupling supports an alternative mechanism[14] for T_e flattening, in which beam-driven CAE dissipates its energy at the resonance location close to the edge of the beam, therefore significantly modifying the energy deposition profile (similar to a mechanism suggested qualitatively for GAEs in Ref. 13).

Both experimental observations and numerical simulations presented here demonstrate that for this particular H-mode NSTX discharge a large number of GAEs and CAEs were excited by the beam ions. The calculated range of the unstable toroidal mode numbers, frequencies, and mode polarizations appears to be reasonably close to experimental observations.[23,24] Linear simulations show multiple unstable CAEs for a range of toroidal mode numbers $n = 4$–9, coupled with KAW on the high field side. Resonance with KAW is located at the edge of CAE well, and just inside beam ion density profile, and the radial width of KAW is determined by the beam ion Larmor radius and $V_A(R)$ scale length as $(L\rho^2)^{1/3}$, where ρ is the effective Larmor radius defined by

Eq. (5). It is shown that localization of KAW on HFS is related to the shape of the CAE effective potential well.

Analysis of the particle phase-space for unstable CAEs shows that the resonant particles have wide range of pitch-angle parameter $\lambda = 0.1$–1.2 and energies $\varepsilon = 10$–60 keV, but a relatively narrow range of resonant $v_\parallel$. While this group includes both passing and trapped particles, the co-CAE instability is shown to be driven by the trapped ions. Beam ion power scan allows estimating a damping rate of CAE due to its linear coupling to KAW, and shows that the CAE instability is close to marginal for the experimental parameters. The CAE/KAW coupling is the main linear damping mechanism for CAE, and the damping rate is $\gamma_{damp} = 0.66\gamma_{dr}$ for the $n = 4$ CAE. This sets up a threshold value of the beam power needed for the excitation of this mode for a given set of NSTX parameters at $P \sim 4$ MW.

A set of nonlinear simulations demonstrate that the CAE instability saturates due to nonlinear particle trapping, which has been confirmed by scaling of the saturation amplitude with the growth rate $\delta B_\parallel \sim \gamma^2$, that is, the instability saturates mainly through the changes in the beam ion distribution function, and field nonlinearities play a minor role. A calculated fraction of NBI energy which can be transferred to single unstable CAE is significant: up to $P \sim 0.4$ MW for one mode with amplitude $\delta B / B_0 \sim 3 \cdot 10^{-3}$. Therefore, this study demonstrates that a large fraction of beam energy can be transferred to several unstable CAEs of relatively large amplitudes and absorbed at the resonant location. Energy flux is shown to be directed away from the magnetic axis (CAE) toward the resonance location (KAW). Absorption rate, calculated as a change in the Poynting flux across the resonance layer, shows a very strong scaling with growth rate (Fig. 13(c)), implying that the energy loss at the resonance scales as a fifth power of the beam power. Calculated magnitude of power absorption is significant enough to have a direct effect on the electron temperature profile. Comparison of CAE/KAW energy channeling mechanism considered here and the earlier study of the enhanced electron transport in the presence of multiple unstable GAEs demonstrate that the scaling of absorption rate with mode amplitude $\Delta S \sim \gamma^5 \sim \delta B^{2.5}$ is weaker than predicted by alternative mechanism, where $\chi \sim \delta B^3$ or $\sim \delta B^6$.[12] At the same time, the presented energy channeling mechanism predicts significant changes in T_e profile at lower and more realistic CAE amplitudes, and does not require a large number of unstable modes as in Ref. 12, where at least 15 modes with amplitudes $\delta B / B_0 \sim 5 \cdot 10^{-3}$ are needed to explain the observed changes in T_e.

Strong CAE/KAW coupling follows from dispersion relation; therefore, the energy channelling mechanism is generic and it applies to any device with unstable CAEs and the related ion cyclotron emission (ICE) observed in tokamaks.[11] The CAEs are generally predicted to be unstable in tokamaks with $V_0 / V_A > 1$;[3] however, a recent set of HYM simulations (a parameter scan performed for a fixed shape of the beam ion distribution function)[39] shows that excitation of a significant number of unstable CAEs with different toroidal mode numbers requires relatively large values of normalized beam injection velocity, $V_0 / V_A > 3$–4. Future work will include investigation of the effects of the beam ion

distribution function on the CAE and GAE instabilities. A more complete description of the mode conversion in NSTX would require inclusion of the thermal ion FLR effects, and two-fluid (finite ω/ω_{ci}) effects, which is beyond the scope of this paper.

In summary, it is found that beam-driven CAE modes in NSTX mode-convert to KAWs, and therefore can channel the energy of the beam ions from the injection region near the magnetic axis to the location of the resonant mode conversion at the edge of the beam density profile. This mechanism provides alternative explanation to the observed reduced heating of the plasma core at high beam power in the NSTX. Detailed comparison of the relative importance of the energy channelling and anomalous electron transport mechanisms will be reported in future publication.

ACKNOWLEDGMENTS

[1]D. Stutman, L. Delgado-Aparicio, N. Gorelenkov, M. Finkenthal, E. Fredrickson, S. Kaye, E. Mazzucato, and K. Tritz, Phys. Rev. Lett. **102**, 115002 (2009).

[2]E. D. Fredrickson, N. Gorelenkov, C. Z. Cheng, R. Bell, D. Darrow, D. Johnson, S. Kaye, B. LeBlanc, J. Menard, S. Kubota, and W. Peebles, Phys. Rev. Lett. **87**, 145001 (2001).

[3]N. N. Gorelenkov, E. Fredrickson, E. Belova, C. Z. Cheng, D. Gates, S. Kaye, and R. White, Nucl. Fusion **43**, 228 (2003).

[4]E. V. Belova, N. N. Gorelenkov, C. Z. Cheng, and E. D. Fredrickson, in *Proceedings of the 30th EPS Conference on Controled Fusion and Plasma Physics*, St. Petersburg, Russia (European Physical Society, Geneva, 2003), Vol. 23A, p. 3.102.

[5]K. Appert, R. Gruber, F. Troyuon, and J. Vaclavik, Plasma Phys. **24**, 1147 (1982).

[6]J. W. Van Dam, G. Y. Fu, and C. Z. Cheng, Fusion Technol. **18**, 461 (1990); available at http://www.ans.org/pubs/journals/fst/a_29282.

[7]S. M. Mahajan, D. W. Ross, and G. L. Chen, Phys. Fluids **26**, 2195 (1983).

[8]S. M. Mahajan, Phys. Fluids **27**, 2238 (1984).

[9]S. M. Mahajan and D. W. Ross, Phys. Fluids **26**, 2561 (1983).

[10]H. M. Smith and E. Verwichte, Plasma Phys. Controlled Fusion **51**, 075001 (2009).

[11]N. N. Gorelenkov, New J. Phys. **18**, 105010 (2016).

[12]N. N. Gorelenkov, D. Stutman, K. Tritz, A. Boozer, L. Delgado-Aparicio, E. Fredrickson, S. Kaye, and R. White, Nucl. Fusion **50**, 084012 (2010).

[13]Y. I. Kolesnichenko, Y. V. Yakovenko, and V. V. Lutsenko, Phys. Rev. Lett. **104**, 075001 (2010).

[14]E. V. Belova, N. N. Gorelenkov, N. A. Crocker, E. D. Fredrickson, and K. Tritz, Phys. Rev. Lett. **115**, 015001 (2015).

[15]A. Hasegawa and L. Chen, Phys. Fluids **19**, 1924 (1976).

[16]J. R. Johnson and C. Z. Cheng, Geophys. Res. Lett. **24**, 1423, doi:10.1029/97GL01333 (1997).

[17]Y. Lin, J. R. Johnson, and X. Y. Wang, J. Geophys. Res. **115**, A04208, doi:10.1029/2009JA014524 (2010).

[18]M. H. Hong, Y. Lin, and X. Y. Wang, Phys. Plasmas **19**, 072903 (2012).

[19]C. F. F. Karney, F. W. Perkins, and Y.-C. Sun, Phys. Rev. Lett. **42**, 1621 (1979).

[20]K. Appert and J. Vaclavik, Plasma Phys. **25**, 551 (1983).

[21]J. A. Heikkinen, T. Hellsten, and M. J. Alava, Nucl. Fusion **31**, 417 (1991).

[22]K. Kommoshvili, S. Cuperman, and C. Bruma, Plasma Phys. Controlled Fusion **45**, 275 (2003).

[23]N. A. Crocker, E. D. Fredrickson, N. N. Gorelenkov, W. A. Peebles, S. Kubota, R. E. Bell, B. P. LeBlanc, J. E. Menard, M. Podesta, K. Tritz, and H. Yuh, in *Proceedings of the 24th IAEA International Conference*, San-Diego, CA (International Atomic Energy Agency, Vienna, 2012), Paper No. EX/P6-02.

[24]N. A. Crocker, E. D. Fredrickson, N. N. Gorelenkov, W. A. Peebles, S. Kubota, R. E. Bell, A. Diallo, B. P. LeBlanc, J. E. Menard, M. Podesta, K. Tritz, and H. Yuh, Nucl. Fusion **53**, 043017 (2013).

[25]E. V. Belova, S. C. Jardin, H. Ji, M. Yamada, and R. Kulsrud, Phys. Plasmas **7**, 4996 (2000).

[26]E. V. Belova, N. N. Gorelenkov, and C. Z. Cheng, Phys. Plasmas **10**, 3240 (2003).

[27]E. V. Belova, N. N. Gorelenkov, E. D. Fredrickson, H. L. Berk, G. J. Kramer, and S. S. Medley, in *Proceedings of the 24th IAEA International Conference*, San-Diego, CA (International Atomic Energy Agency, Vienna, 2012), Paper No. TH/P6-16.

[28]S. E. Parker and W. W. Lee, Phys. Fluids B **5**, 77 (1993).

[29]R. V. Budny, Nucl. Fusion **34**, 1247 (1994).

[30]E. D. Fredrickson, N. N. Gorelenkov, M. Podesta, A. Bortolon, N. A. Crocker, S. P. Gerhardt, R. E. Bell, A. Diallo, B. LeBlanc, F. M. Levinton, and H. Yuh, Phys. Plasmas **20**, 042112 (2013).

[31]N. A. Crocker, "Density perturbation mode structure of high frequency compressional and global Alfvén eigenmodes in the National Spherical Torus Experiment using a novel reflectometer analysis technique," Nucl. Fusion (unpublished).

[32]V. S. Belikov, Y. I. Kolesnichenko, and R. B. White, Phys. Plasmas **10**, 4771 (2003).

[33]J. B. Lestz, "Hybrid simulations of sub-cyclotron Alfvén Eigenmode stability in spherical tokamaks," Phys. Plasmas (unpublished).

[34]A. Gila, J. Segurab, and N. M. Temme, J. Approx. Theory **120**, 253 (2003).

[35]E. D. Fredrickson, N. Gorelenkov, E. Belova, N. Crocker, S. Kubota, G. Kramer, B. LeBlanc, R. Bell, M. Podesta, H. Yuh, and F. Levinton, Nucl. Fusion **52**, 043001 (2012).

[36]N. A. Crocker, K. Tritz, R. B. White, E. D. Fredrickson, and N. N. Gorelenkov, in *Bulletin of the American Physical Society*, San Jose, CA (2016), Vol. 61, p. NP10.00020.

[37]E. D. Fredrickson, N. N. Gorelenkov, M. Podesta, A. Bortolon, S. P. Gerhardt, R. E. Bell, A. Diallo, and B. LeBlanc, Nucl. Fusion **54**, 093007 (2014).

[38]S. Tang, N. A. Crocker, T. A. Carter, E. Fredrickson, N. Gorelenkov, and W. Guttenfelder, in *Bulletin of the American Physical Society*, San Jose, CA (2016), Vol. 61, p. NP10.00019.

[39]J. B. Lestz, E. V. Belova, and N. N. Gorelenkov, in *Bulletin of the American Physical Society*, 2015, Vol. 60, p. 146.